NJC

Accepted Manuscript

This is an *Accepted Manuscript*, which has been through the Royal Society of Chemistry peer review process and has been accepted for publication.

Accepted Manuscripts are published online shortly after acceptance, before technical editing, formatting and proof reading. Using this free service, authors can make their results available to the community, in citable form, before we publish the edited article. We will replace this *Accepted Manuscript* with the edited and formatted *Advance Article* as soon as it is available.

You can find more information about *Accepted Manuscripts* in the Information for Authors.

Please note that technical editing may introduce minor changes to the text and/or graphics, which may alter content. The journal's standard Terms & Conditions and the Ethical guidelines still apply. In no event shall the Royal Society of Chemistry be held responsible for any errors or omissions in this *Accepted Manuscript* or any consequences arising from the use of any information it contains.

ROYAL SOCIETY OF CHEMISTRY

www.rsc.org/njc

Journal Name

RSCPublishing

ARTICLE

Multi-component assembly and luminescence tuning of lanthanide hybrids through the inside-outside double modification of zeolite A/L

Cite this: DOI: 10.1039/x0xx00000x

Lei Chen, Bing Yan*

Received 00th January 2012,
Accepted 00th January 2012

DOI: 10.1039/x0xx00000x

www.rsc.org/

A series of novel multi-component photofunctional hybrid materials are assembled by lanthanide polyoxometalates ($Na_9LnW_{10}O_{36}\cdot 32H_2O$, LnW10, Ln = Eu, Tb, Sm and Dy), ionic liquids (IMCl) and functionalized zeolite A/L through an inside-outside double modification path. Firstly, zeolite A/L is functionalized with lanthanide complexes (Eu-TTA or Tb-TAA) by the ion-exchange treatment and "ships in a bottle" dispersion. Then, 1-methyl-3-(trimethoxysilylpropyl) chloride (IM^+Cl^-) is covalently grafted onto the functionalized zeolite A/L and linked to lanthanide polyoxometalates as a double linker. These hybrids own two luminescence centers, one is lanthanide complexes, and the other is lanthanide polyoxometalates. By adjusting the different components of the hybrids, it can realize the luminescent tuning and integration of various colors (white, warm-white, green and red light). These results can be expected to have potential application in practical fields.

Introduction

Lanthanide-based organic-inorganic hybrid materials have attracted great attention from many researchers in recent two decades for their attracting mechanical property, high thermal-stability and luminescence features (photo-stability, high luminescence quantum yield, long lifetime emission and high color purity).[1] So they have versatile potential applications in practical fields such as luminescent thin films, polymeric optical amplifiers, lasers, OLEDs, luminescent chemical sensors and luminescent molecular thermometers, *etc*.[2,3] Within these kinds of hybrid materials, lanthanide complexes or lanthanide-doped nanoparticles are incorporated into inorganic hosts, like MCM-41, SBA-15 or zeolite,[4-6] or organic polymer matrices.[7] Zeolite A/L is crystalline microporous materials with highly regular nanometer-sized channels or cavities inside, which has been successfully employed to obtain highly organized arrangements of a large variety of organo-lanthanide complexes via the "ship in a bottle method".[8] Zeolite A/L has proved to be an ideal host material for luminescent guest species because it can offer an effective protection of guests and maintain photoluminescence properties during the annealing process at 973 K under air atmosphere.[9] Zeolite A/L can be further modified with targeting groups for its surface is covered with a large amount of Si-OH.[10]

Ionic liquids (ILs) are composed entirely of cations and anions and can melt around 373 K or below a convenient, arbitrary temperature limit.[11] Little attention has been paid to the application of these purely inorganic ionic liquids for a long time until the water-stable and air-stable ionic liquids have been synthesized by Wilkes and Zaworotko in 1992,[12] so that they begin to be widely explored as solvents or reactant in synthetic chemistry. These salts possess many outstanding properties, such as thermal stability, non-volatility, non-flammability, high electrical conductance and negligible vapor pressure, *etc*.[13] Besides, soft material with intense photoluminescence can be obtained by dissolving Ln_2O_3 and organic ligand into a task-specific ionic liquid.[14] Furthermore, environment friendly ionic liquids have only a yellowish color are used as excellent organically linkage.[15]

Polyoxometalates (POMs) are inorganic metal oxide clusters formed by some transition metal ions in their highest oxidation state, whose crystalline framework structure makes.[16] POMs also exhibit wealthy physical properties such as optics, electrics and magnetics, which are favorable for the hybrid materials.[17] $[LnW_{10}O_{36}]^{9-}$ (Ln = Eu, Tb, Sm, Dy) anion is made up of Ln^{3+} ion and $[W_5O_{18}]^{6-}$ fragments (five WO_6 octahedra sharing edges). It is generally known that LnW10 shows outstanding luminescent performance such as high luminescent quantum yields and long luminescent lifetimes, especially $[EuW_{10}O_{36}]^{9-}$ (EuW10) has been discovered by Weakley and Peacock and exhibits the best luminescent nature.[18] Fabricating it into hybrid materials can effectively keep the thermal and luminescent stability of LnW10. The hybrids of ionic liquid encapsulated LnW10 anions through electrostatic force can be easily assembled have aroused great interest of many researchers.[19,20]

In this paper, we put forward a novel inside-outside double modification path to prepare a series of multi-component lanthanide hybrid materials. Both organo-lanthanide complexes and LnW10 are used as the luminescent species through two functionalizing processes. Lanthanide complexes are firstly incorporated into the nanometer-sized channels or cavities of Zeolite A/L, and then it is modified with 1-methyl-3-(trimethoxysilylpropyl) chloride as

grafted linker as well to interact with PMOs through ion exchange. Subsequently, nine hybrid materials LnW10-IM-[ZA/L⊃Eu-TTA] or LnW10-IM-[ZA/L⊃Tb-TAA] (Ln = Eu, Tb, Sm, Dy) are obtained, whose physical characterization and especially the photophysical properties are discussed in detail.

Experimental section

Starting materials. Chemical pure and highly crystalline Zeolite A/L (ZA/L) crystals were synthesized according to the previously reported procedure.[21] All solvents and reagents were analytically pure without further purification. Sodium hydroxide, potassium hydroxide, sodium meta-aluminate were from Aladdin and colloidal silica (40 %, Ludox HS-40) was from Sigma. (3-Chloropropyl) trimethoxysilane (99 %), 1-methyl imidazole (99 %), theno-yltrifluoroacetone (99 %, TTA) and 1,1,1-trifluoroacetylace-tone (98 %, TAA) were purchased from Adamas. $LnNO_3{\cdot}xH_2O$ (Ln = Eu/Tb/Sm/Dy) were obtained by dissolving their respective oxides (Eu_2O_3, Tb_4O_7, Sm_2O_3 and Dy_2O_3) in concentrated nitric acid (69.2 %). Other chemicals were analytically pure and purchased from China National Medicines Group and used as received.

Synthetic procedures

Synthesis of polyoxometalates (LnW10, $Na_9LnW_{10}O_{36}{\cdot}32H_2O$). $LnW_{10}O_{36}^{9-}$ can be abbreviated to LnW10 (Ln = Eu/Tb/Sm/Dy). $Na_9LnW_{10}O_{36}{\cdot}32H_2O$ was prepared according to the method reported by Peacock and Weakley.[18] $Na_2WO_4{\cdot}2H_2O$ was dissolved in 10 mL deionized water, the solution was heated to 358 K, and then adjust the pH value was adjusted to 7.2 with glacial acetic acid. A total of 0.8 mL $Ln(NO_3)_3{\cdot}6H_2O$ (0.8 M) was then added dropwise by stirring, and a large amount of white precipitate immediately generated. After the solution was cooled naturally to room temperature, colorless crystals were obtained. Finally, the product were collected by centrifugation, washed with distilled water three times, and dried in air conditions for 24 h. The colorless crystals are LnW10.

Synthesis of ionic liquid (IM^+Cl^-). Highly purified 1-methyl-3-(trimethoxysilylpropyl) chloride (IM^+Cl^-) was synthesized according to previous literature.[22] Equal molar amounts of 1-methyl imidazole (0.820 g, 10 mmol) with (3-chloropropyl) trimethoxysilane (1.987 g, 10 mmol) were put together in a round-bottom flask with magnetic stirring, a little toluene was added to remove atmosphere and water vapor, and then the pale-yellow sticky and transparent liquid solution was obtained by stirring for 3 days at 343 K in an argon atmosphere. The coarse product was washed with ethyl acetate by three times to clean unwanted substances, and then taken down on a rotary evaporator to remove excess solvent to obtain ionic liquid, referred to as IM^+Cl^-. ^1H NMR ($CDCl_3$, 400 MHz): 10.15 (1H, s), 7.52 (1H, s), 7.30 (1H, s), d 4.11 (2H, t), 3.82 (3H,s), 3.29 (9H, s), 1.82 (2H, m), 0.99 (2H,t).

Synthesis of ZA/L⊃Eu-TTA and ZA/L⊃Tb-TAA. Ln-ZA/L samples were synthesis according to the ion-exchange as follows.[23] A certain amount of ZA/L was added to 20 mL deionized water, then 0.6 mL of a 0.10 M aqueous solution of $EuCl_3$ or $TbCl_3$ was added and heated at 353 K for 12 h. After cooling to room temperature, the product was washed with copious amounts of deionized water by three times and then dried for 5 h at 353 K. Neutral dyes such as TTA and TAA were inserted from the gas phase by using the "ship in a bottle" method. Ln-ZA/L was firstly placed in an ampoule, and was degassed and dried at 423 K for 2 h to get rid of the solvent molecules and water molecules. The reaction time and temperature were 18 h at 453 K for TTA and 18 h at 353 K for TAA. The product obtained was washed with CH_2Cl_2 by several times, and dried for 5 h at 323 K in a vacuum. Selected elemental analyses data were determined for some systems: ZA⊃Eu-TTA: Eu 3.23 %, C 5.11 %, H 0.20 %; ZA⊃Tb-TAA: Tb 3.86 %, C 4.35 %, H 0.23 %; ZL⊃Tb-TAA: Tb 3.50 %, C 4.00 %, H 0.20 %. This suggested that the functionalized zeolite can be realized. The content of C and H is with the molar ratio C: H of about 2:1 (ZA⊃Eu-TTA) or 1:1 (ZA/ZL⊃Eu-TAA), revealing the of TTA (C10: H5) and TAA (C5: H5) system.

Preparation of LnW_{10}-IM-[ZA/L⊃Eu-TTA] or LnW_{10}-IM-[ZA/L⊃Tb-TAA] (Ln = Eu, Tb, Sm, Dy). 100 mg of modified zeolite (ZA/L⊃Eu-TTA and ZA/L⊃Tb-TAA) was suspended in 20 mL of toluene solution, then 0.3 mmol of IM^+Cl^- were added and heated at 353 K. After 18 h, the surface-inserting chloropropylsilyl-imidazole covalently bonded microporous silica through Si–O linkage. 0.05 mmol of LnW10 was then transferred into the solution and keep heating for 24 h. Finally products were collected by rotary evaporation, washed with cyclo-hexane several times, and dried under vacuum, which can be abbreviated to LnW10-IM-[ZA/L⊃Eu-TTA] or LnW10-IM-[ZA/L⊃Tb-TAA] (Ln = Eu, Tb, Sm, Dy). The selected contents of Ln, W and C, H element can be determined. For EuW10-IM-[ZA⊃Eu-TTA]: Eu 3.30 %, W 19.6 %, C 3.05 %, H 0.18 %; for EuW10-IM-[ZA⊃Tb-TAA]: Eu 1.60 %, Tb 1.80 %, W 19.0 %, C 3.80 %, H 0.20 %; for EuW10-IM-[ZL⊃Tb-TAA]: Eu 1.80 %, Tb 1.65 %, W 21.0 %, C 3.70 %, H 0.20 %. According to these data, it can be predicted the molar ratios of Eu: W for EuW10-IM-[ZA⊃Tb-TAA] and EuW10-IM-[ZL⊃Tb-TAA] are close to 1:10. Besides, the content of Tb^{3+} also suggested Tb^{3+} functionalized ZA/ZL. Comparing to the C, H content of ZA⊃Eu-TTA and ZA/ZL⊃Eu-TAA, the increase of C and H content may be due to the introduction of IM.

Physical characterization. X-ray powder diffraction patterns (XRD) were recorded on Rigaku D/max-Rb diffractometer equipped with Cu anode, and data were collected within the 2θ range of 5–60 °. The contents of Ln^{3+} ions (Ln = Eu, Tb) and W in the hybrids were determined with ICP-AES. The elemental analyses of C, H element the hybrids are measured with a CARIO-ERBA 1106 elemental analyser. Scanning electronic microscope (SEM) images were obtained by a Hitachi S-4800. Fourier transform infrared spectra (FTIR) were gained on a Nexus 912 AO446 infrared spectrum radiometer using KBr slices for solid samples, measured within from the 4000 to 400 cm^{-1} region. ^1H NMR spectra were acquired in $CDCl_3$ on a BRUKER ARX400 spectrometer with tetramethylsilane (TMS) as the inter reference. Luminescence (excitation and emission) spectra and luminescence lifetime measurements of the solid samples were recorded on an Edinburgh FLS920 spectrophotometer, using a Xenon lamp as the excitation source, whose powers are 450 W and 100 mW, respectively. And the outer luminescent quantum efficiency was determined using an integrating sphere (150 mm diameter, $BaSO_4$ coating) from an Edinburgh FLS920

phosphorimeter. All photoluminescence spectra have been recorded at room temperature.

Results and discussion

Figure 1 shows the schematic representation and synthesis process of hybrid materials LnW10-IM-[ZA/L⊃Eu-TTA] and LnW10-IM-[ZA/L⊃Tb-TAA] (Ln = Eu/Tb/Sm/Dy). Though it is hard to determine their exact structures and is even hardly possible to confirm the coordinate environment of lanthanide ions, the main structures of hybrid materials is predictable to a certain extent by the lanthanide coordination chemistry principle. The single chemical modification of ionic liquid exchanged POMs and ionic liquid covalently bonded hybrids are both proved to be practical by the reported works.[15] Besides, single lanthanide ions functionalized zeolite and further introduction of ligands by gas dispersion (ship-in-bottle) are also practical by the reported works.[10,14] IM^+ plays an important role in the final structure, for the reason that it not only grafted onto modified microporous silica zeolite A/L (ZA/L) for its alkoxy groups to form Si–O linkage but it also can interact with LnW10 through ion exchange with electrostatic force. We prepare ionic liquid functionalized LnW10 by adding the appropriate proportion of LnW10 according to the amount of mole IM^+, and they possess one unit of negative charge and nine units of positive charge, respectively.

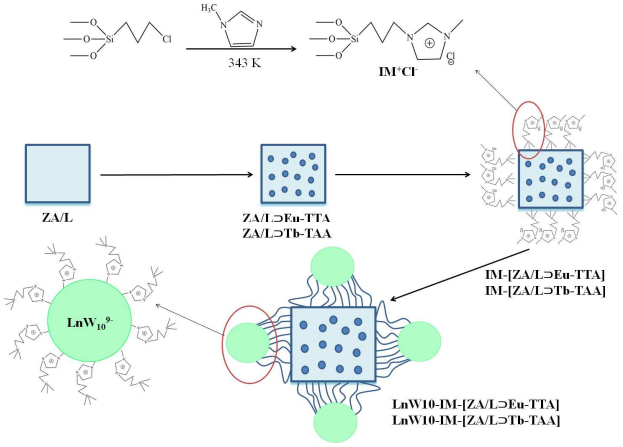

Figure 1 The schematic representation and synthesis process of hybrid materials LnW10-IM-[ZA/L⊃Eu-TTA] and LnW10-IM-[ZA/L⊃Tb-TAA] (Ln = Eu/Tb/Sm/Dy)

Figure S1 exhibits the X-ray diffraction (XRD) analysis of zeolite A (ZA, a) and zeolite L (ZL, b) from 5-60 ° in a 2θ range. Comparing with the standard JPCDS card, it is found that the outstanding framework structure of crystals is synthesized. ZA is formed by $[AlO_4]^{5-}$ and $[SiO_4]^{4-}$ tetrahedra linked via bridging oxygen atoms, whose three-dimensional network of cavities have a smallest free diameter of about 0.41 nm and the largest free diameter being 1.14 nm. ZL is a crystal with a rigid three-dimensional framework of tetrahedral $[AlO_4]^{5-}$ and $[SiO_4]^{4-}$ primary building units, which consists of cancrinite cages (Î-cage) linked by double 6-rings (D6R) contributed to ZL's one-dimensional channels running along the c-axis of the hexagonal crystals. The channels or cavities of ZA/L are easily chemically modified and can be conveniently entrapped inside.

Figure S2 shows the selected FTIR spectrum of SmW10-IM-[ZA⊃Eu-TTA]. The broad and strong peak from the region about 3100 to 3600 cm^{-1} can be ascribed to the stretching vibration of O–H group which are of extremely rich on the surface of the zeolite A. The absorption peak around 1012 cm^{-1} corresponds to the anti-symmetric stretching vibrations of Si-O and Al-O bond in primary tetrahedral building units, and it is attributed to the occurrence of cohydrolysis and copolycondensation process. The peaks whose absorption peaks locating at 1635, 1574, 1456 cm^{-1} can be ascribed as ring stretching of the imidazolium ring in IM. And the water molecules present in the samples also contribute to the big absorption band at 1635 cm^{-1} by the bending vibrations. In addition, a series of absorption bands at 2963 and 2900 cm^{-1} correspond to the methylene ($-CH_2-$) groups in IM. It indicates that IM has been grafted onto the host of ZA. The peak located at 466 cm^{-1} corresponds to the bending vibration of Si-O-Si, weak band centered at 966 cm^{-1} are due to silanol (Si-OH) stretching vibrations of surface groups.

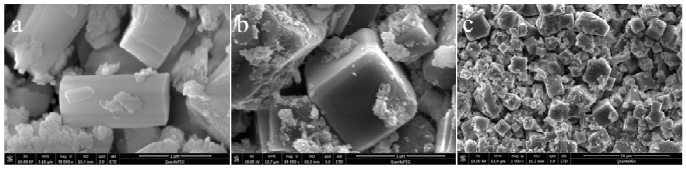

Figure 2 The selected SEM images of TbW10-IM-[ZL⊃Eu-TTA] (a) and SmW10-IM-[ZA⊃Tb-TAA] (b, c)

The selected SEM images of TbW10-IM-[ZL⊃Eu-TTA] (a) and SmW10-IM-[ZA⊃Tb-TAA] (b, c) are shown in Figure 2. Figure 2 (a) illustrates the cylinder-shape of the functionalized ZL with a length between 1000 and 2000 nm and a diameter in the order of 500 nm. There are several mass of TbW10 relative evenly distributed on the surface of ZL, which directly proves that TbW10 and ZL are linked by IM^+. SEM images of SmW10-IM-[ZA⊃Tb-TAA] are given in Figure 2 (b, c), in which we can see the shape morphology of ZA no longer have the same morphology as precursor. By the coordination effect and electrostatic force of IM^+, SmW10 and ZA formed a mix of new complex material. Figure 2 (c) is the selected macro SEM picture of SmW10-IM-[ZA⊃Tb-TAA], showing that SmW10 has a clear impact on the inclusion of modified ZA. This takes agreement with the FT-IR spectra.

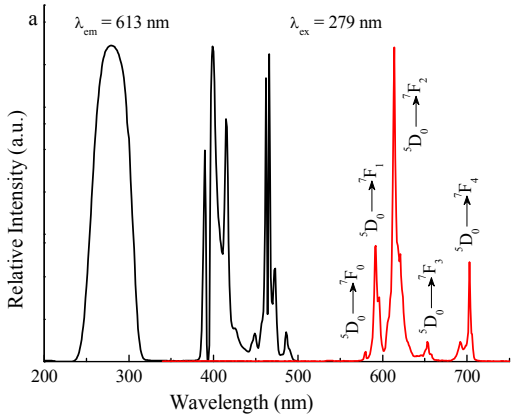

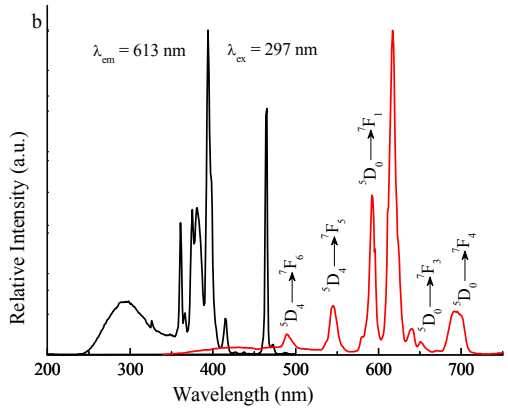

Figure 3 The excitation and emission spectra of hybrids EuW10-IM-[ZA ⊃ Eu-TTA] (a) and EuW10-IM-[ZA ⊃Tb-TAA] (b).

Figure 3 shows the excitation and emission spectra of EuW10-IM-[ZA⊃Eu-TTA] (a) and EuW10-IM-[ZA⊃Tb-TAA] (b). The excitation spectrum of EuW10-IM-[ZA⊃Eu-TTA] is monitored at 613 nm. A broad band ranging from 240 to 310 nm centered at 278 nm can be found, which can be ascribed to the ligands-metal charge transfer (LMCT) of O→W and implies the energy transfer from $[W_5O_{18}]^{6-}$ to Eu^{3+}. The charge transfer band plays an important role in its luminescence. The absorption bands of TAA and the host of ZA are relatively weak can be hidden in the big band. There are several absorption lines in the excitation are assigned to the f-f transitions and the characteristic peaks of Eu^{3+} situate at 390 nm ($^7F_0\rightarrow{}^5F_6$), 399 nm ($^7F_0\rightarrow{}^5F_6$), 415 nm ($^7F_0\rightarrow{}^5D_3$), 461 nm and 466 nm ($^7F_0\rightarrow{}^5D_2$), respectively. However, the excitation spectrum of EuW10-IM-[ZA⊃Eu-TTA] shows a strong wide band and some strong characteristic peaks of Eu^{3+}. Emission spectrum is observed upon excitation at 298 nm. These peaks are come from transitions within the $4f^6$-electron shell of Eu^{3+} and ascribed to energy level transitions Eu^{3+} from $^5D_0$ metastable state to terminal levels, respectively. The characteristic transition of Eu^{3+} (580 nm, $^5D_0\rightarrow{}^7F_0$; 592 nm, $^5D_0\rightarrow{}^7F_1$; 614 nm, $^5D_0\rightarrow{}^7F_2$; 654 nm, $^5D_0\rightarrow{}^7F_3$; 703 nm, $^5D_0\rightarrow{}^7F_4$) can be observed. And the obvious inclination of red-shift in $^5D_0\rightarrow{}^7F_{0\text{-}4}$ transition can be an evidence of the increase in the covalency of the Eu^{3+}-ligand bonds inside of ZA, and supporting the existence of an ordinal scale of covalency. The $^5D_0\rightarrow{}^7F_0$ transition standing for the symmetric forbidden emission is uneasy to be noticed. And the intensity ratio of $^5D_0\rightarrow{}^7F_2$ transition to that of $^5D_0\rightarrow{}^7F_1$ transition (I_{02}/I_{01}) could be used as a response of the polarizable chemical environment around Eu^{3+} ion. Compared to parent Na_9EuW10 ($I_{02}/I_{01}\approx 0.85$), Eu^{3+} in the hybrids has more complicated chemical environment. The luminescence data of EuW10-IM-[ZA⊃Tb-TAA] are shown in Figure 3 (b). The excitation spectrum monitored at 613 nm shows a broad band ranging from 230 to 325 nm peaking at 297 nm, which can be ascribed to the ligands-metal charge transfer (LMCT) of O→W and the host of ZA. And there are also some strong characteristic transition of Eu^{3+} (361 nm, $^7F_0\rightarrow{}^5D_4$; 375 nm, $^7F_0\rightarrow{}^5G_4$; 381 nm, $^7F_0\rightarrow{}^5G_3$; 394 nm, $^7F_0\rightarrow{}^5L_6$; 415 nm, $^7F_0\rightarrow{}^5D_3$; 466 nm, $^7F_0\rightarrow{}^5D_2$) can be observed. And the characteristic peaks of Tb^{3+} are relatively weak can't be find in the spectrum. The luminescence spectrum of EuW10-IM-[ZA⊃Tb-TAA] was measured by excitation at 317 nm. Several characteristic transition of Tb^{3+} (489 nm, $^5D_4\rightarrow{}^7F_6$; 545 nm, $^5D_4\rightarrow{}^7F_5$) and Eu^{3+} (592 nm, $^5D_0\rightarrow{}^7F_1$; 651 nm, $^5D_0\rightarrow{}^7F_3$) are observed, respectively. And the characteristic peak at 617 nm may be the overlap of Eu^{3+} (613 nm, $^5D_0\rightarrow{}^7F_2$) and Tb^{3+} (622 nm, $^5D_4\rightarrow{}^7F_3$). The Eu^{3+} ion has a serious chemical environment that it's displayed I_{02}/I_{01} values is 2. There is also a narrow band at 692-701 nm (Eu^{3+} $^5D_0\rightarrow{}^7F_4$) is stronger than general europium complexes. These results overlap with the luminescent performance of parent EuW10.

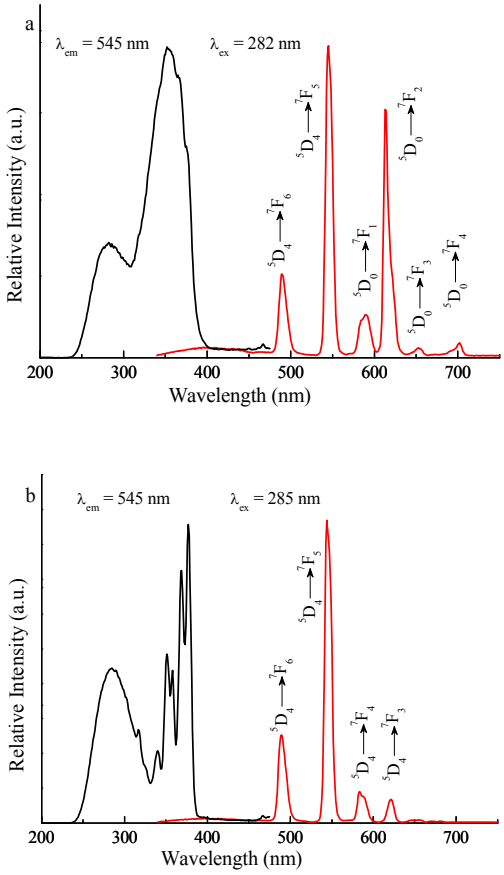

Figure 4 The luminescence spectra of hybrids TbW10-IM-[ZA⊃Eu-TTA] (a) (λ_{em} = 613 nm, λ_{ex} = 282 nm) and TbW10-IM-[ZA⊃Tb-TAA] (b) (λ_{em} = 613 nm, λ_{ex} = 285 nm)

Figure 4 exhibits the luminescence spectra of TbW10-IM-[ZA⊃Eu-TTA] (a) and TbW10-IM-[ZA⊃Tb-TAA] (b), respectively. In the excitation spectrum of TbW10-IM-[ZA⊃Eu-TTA], two broad bands appear about from 240 to 310 nm peaking at 282 and 310 to 400 nm centered at 352, respectively. The former band can be ascribed to the LMCT of O→W, implying that the energy transfer occurs from $[W_5O_{18}]^{6-}$ to Tb^{3+}, and the latter band is assigned to the interaction between TTA and Eu^{3+} ions. But the line absorption to the f–f transition of Eu^{3+} and Tb^{3+} is present at a low intensity. The emission spectrum is excited at 282 nm. There are two sharp emission lines at 490 and 545 nm, which can be ascribed to the $^5D_4\rightarrow{}^7F_6$ and $^5D_0\rightarrow{}^7F_5$ transitions of Tb^{3+}, respectively. And the characteristic peaks at 589, 613, 653 and 702 nm attributed to the f–f transition of Eu^{3+} ($^5D_0\rightarrow{}^7F_1$, $^5D_0\rightarrow{}^7F_2$, $^5D_0\rightarrow{}^7F_3$ and $^5D_0\rightarrow{}^7F_4$). The

characteristic sharp bands at 489 nm should be the overlap of Tb^{3+} (587 nm, $^5D_4 \rightarrow {}^7F_4$) and Eu^{3+} (592 nm, $^5D_0 \rightarrow {}^7F_1$). When compared with these characteristic peaks, we can find that the intensity of Tb^{3+} characteristic peaks are higher than that of Eu^{3+}'s. The excitation spectrum (λ_{em} = 545 nm) of TbW10-IM-[ZA⊃Tb-TAA] is shown in Figure 4 (b). We can see a broad band (250-330 nm) and five sharp absorption lines at 340, 351, 358, 369 and 377 nm. The broad band centered 285 nm can be ascribed to the π-π^* electron transition of TAA and the O → W, and the latter is stronger. By monitoring the emission spectrum at 317 nm, we can see four characteristic sharp bands at 489, 544, 584 and 621 nm attributed to $^5D_4 \rightarrow {}^7F_J$ (J = 6, 5, 4, 3), respectively. And in TbW10-IM-[ZA⊃Tb-TAA] hybrid materials, $^5D_4 \rightarrow {}^7F_5$ transition of europium ions is the most prominent.

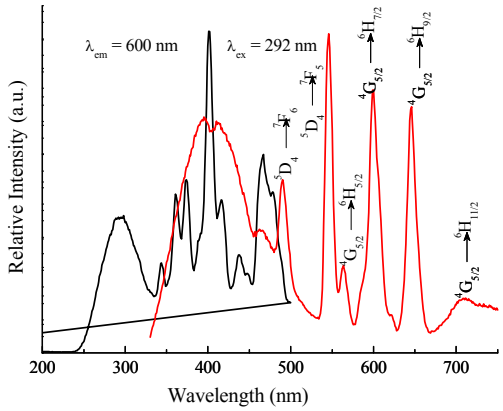

Figure 5 The excitation and emission spectra of SmW10-IM-[ZA⊃Tb-TAA]

Figure 5 shows the luminescence spectra of SmW10-IM-[ZA⊃Tb-TAA]. A broad band (250-330 nm) centered at 298 nm can be observed in the excitation spectrum, which is due to the LMCT of O→W of SmW10. The characteristic transitions of Sm^{3+} and Tb^{3+} are checked. The emission spectrum monitored at 292 nm shows a strong band from 330 to 480 nm centered at 396 and 410 nm to the host of ZA. Other two sharp bands at 490 and 546 nm due to the transition of $^5D_4 \rightarrow {}^7F_6$ and $^5D_4 \rightarrow {}^7F_5$, respectively. The transition $^4G_{5/2} \rightarrow {}^6H_{5/2}$, $^4G_{5/2} \rightarrow {}^6H_{7/2}$, $^4G_{5/2} \rightarrow {}^6H_{9/2}$ and $^4G_{5/2} \rightarrow {}^6H_{11/2}$ result in the characteristic wide peak of 564, 600, 646 and 709 nm. Among these emission bands, the transition $^4G_{5/2} \rightarrow {}^6H_{5/2}$ has the highest intensity.

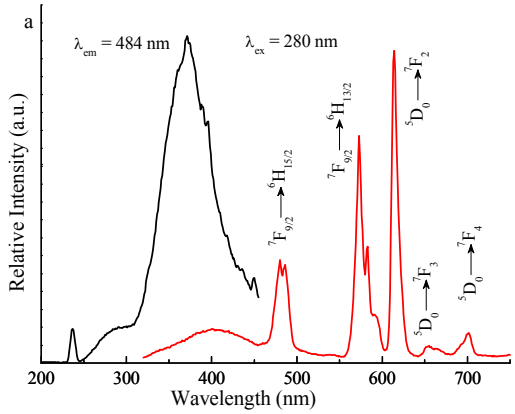

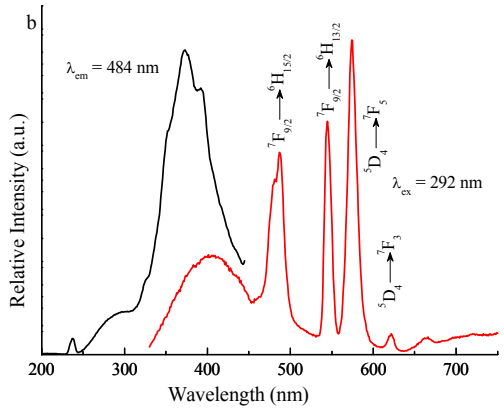

Figure 6 The excitation and emission spectra of hybrids DyW10-IM-[ZA⊃Eu-TTA] (a) (λ_{em} = 484 nm, λ_{ex} = 280 nm) and DyW10-IM-[ZA⊃Tb-TAA] (b) (λ_{em} = 484 nm, λ_{ex} = 292 nm)

The luminescent data of DyW10-IM-[ZA⊃Eu-TTA] and DyW10-IM-[ZA⊃Tb-TAA] are shown in Figure 6. The excitation spectrum of DyW10-IM-[ZA⊃Eu-TTA] in Figure 6 (a) is measured by monitoring the $^7F_{9/2} \rightarrow {}^6H_{15/2}$ transition at 484 nm. A narrow band from 250-300 nm is lower than the strong broad band from 300-450 nm, implying that the relative intensity of characteristic excitation lines of the Eu^{3+} and Dy^{3+} f–f transitions is more intense than the LMCT of O→W of DyW10. The appearance of band centered at 371 nm may be probably related to a superposition with host broad emission as well. Emission spectrum shows a weak wide band from 320-450 nm and five bands of emission transitions. DyW10 leads to the split of $^7F_{9/2} \rightarrow {}^6H_{15/2}$, $^7F_{9/2} \rightarrow {}^6H_{13/2}$ transitions. The transitions at $^7F_{9/2} \rightarrow {}^6H_{15/2}$ divide from 578 to 583 nm, another transition $^7F_{9/2} \rightarrow {}^6H_{13/2}$ break into emission region from 480 nm to 486 nm. And the characteristic transition of Eu^{3+} at 614, 655 and 701 nm ascribed to the transition of $^5D_0 \rightarrow {}^7F_2$, $^5D_0 \rightarrow {}^7F_3$ and $^5D_0 \rightarrow {}^7F_4$, respectively. Figure 6 (b) exhibits the luminescence spectrum of DyW10-IM-[ZA⊃Tb-TAA]. A weak band from 250-310 nm attributed to the LMCT of O→W of DyW10. Another strong band from 310 to 440 nm is corresponded to the emission of ZA and the interaction between TAA. A complicated emission spectrum monitored at 292 nm is composed of a broad weak band from 330 to 450 nm located in visible region, and five characteristic strong peaks. The blue luminescence at 484–495 nm is ascribed to the split of $^7F_{9/2} \rightarrow {}^6H_{15/2}$ transition in DyW10. Among these emission bands, the transition $^7F_{9/2} \rightarrow {}^6H_{13/2}$ has the highest intensity located at 574 nm due to blue shift phenomenon appears. Moreover, the characteristic emission lines of Tb^{3+} (545 nm, $^5D_4 \rightarrow {}^7F_5$; 622 nm, $^5D_4 \rightarrow {}^7F_3$) can be observed.

Figure 7 shows the luminescence spectra of lanthanide hybrids based with ZL. The excitation spectrum of EuW10-IM-[ZL⊃Tb-TAA] (Figure 7 (a)) is shown by monitoring the $^5D_0 \rightarrow {}^7F_2$ transition at 613 nm. A broad band ranging from 250 to 355 nm centered at 272 nm and 318 nm can be observed, which can be ascribed to the LMCT of O→W for the energy transfer from TTA to the Eu^{3+} ions. Several sharp absorption lines are assigned to transition of Eu^{3+} at 362 nm ($^7F_0 \rightarrow {}^5D_4$), 376 nm ($^7F_0 \rightarrow {}^5G_4$), 381 nm ($^7F_0 \rightarrow {}^5G_3$), 394 nm ($^7F_0 \rightarrow {}^5F_6$), 416 nm ($^7F_0 \rightarrow {}^5D_3$) and 464 nm ($^7F_0 \rightarrow {}^5D_2$), respectively.

The emission spectrum is monitored by excitation at 318 nm. The corresponding emission spectrum consists of several prominent lines at 490, 545, 582, 592, 614-621, 634, 654, 693-703 nm. Tungstate leads to the split of $^5D_0 \rightarrow {}^7F_2$, $^5D_0 \rightarrow {}^7F_4$ transitions (EuW10). The transition $^5D_0 \rightarrow {}^7F_2$ at 613 nm is divided from 614 to 621 nm, another transition $^5D_0 \rightarrow {}^7F_4$ at 700 nm split from 693 nm to 703 nm. In the emission spectrum, the characteristic emissions of Eu^{3+} (582 nm, $^5D_0 \rightarrow {}^7F_0$; 593 nm, $^5D_0 \rightarrow {}^7F_1$; 654 nm, $^5D_0 \rightarrow {}^7F_3$) and Tb^{3+} (490 nm, $^5D_4 \rightarrow {}^7F_6$; 545 nm, $^5D_4 \rightarrow {}^7F_5$; 634 nm, $^5D_4 \rightarrow {}^7F_3$) can be observed. The EuW10 have an important influence on width, position and shapes of the luminescent peaks. The luminescence features of TbW10-IM-[ZL⊃Eu-TTA] (b) are presented in Figure 7 (b). In the excitation spectrum, a broad band centered at 318 m with a shoulder at 277 nm was observed, which is the characteristic absorption of TTA due to the π–π* electron transition and the shoulder is ascribed to the ligands-metal charge transfer (LMCT) of O → W. The characteristic transition of Eu^{3+} and Tb^{3+} can be observed, as well. In the emission spectrum, characteristic transition of Eu^{3+} (589 nm, $^5D_0 \rightarrow {}^7F_1$; 613 nm, $^5D_0 \rightarrow {}^7F_2$; 654 nm, $^5D_0 \rightarrow {}^7F_3$; 701 nm, $^5D_0 \rightarrow {}^7F_4$) and Tb^{3+} (489 nm, $^5D_4 \rightarrow {}^7F_6$; 544 nm, $^5D_4 \rightarrow {}^7F_5$) are observed, respectively.

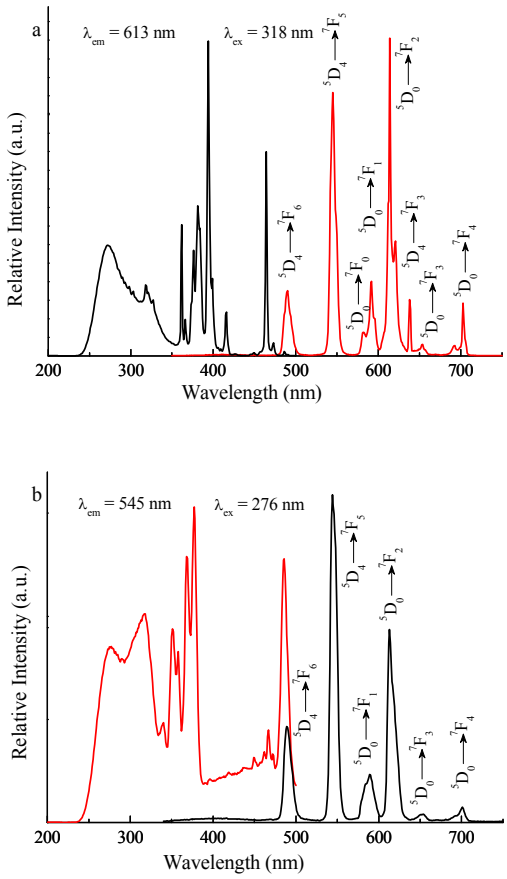

Figure 7 The luminescent spectra of hybrids EuW10-IM-[ZL⊃Tb-TAA] (a) and TbW10-IM-[ZL⊃Eu-TTA] (b)

Furthermore, the corresponding CIE coordinate diagrams of the hybrid materials are shown in Figure 8 and Figure S3. Figure 8 (a) for SmW10-IM-[ZA⊃Tb-TAA] (λ_{ex} = 285 nm) is situated in the white region, whose CIE coordinate is x = 0.3095, y = 0.2774. Figure 8 (b) for TbW10-IM-[ZL⊃Eu-TTA] emits close white luminescence, whose CIE coordinate is in the warm white region, which is useful for lighting. For EuW10-IM-[ZA⊃Eu-TTA] hybrids in Figure 8 (c), the dominant emission of Eu^{3+} produces the luminescent color in red region (0.6578, 0.3357). Figure 8 (d) for TbW10-IM-[ZA⊃Tb-TAA] is located in green region, whose CIE coordinate is x = 0.2959, y = 0.5793. The intense emission of Tb^{3+} is of benefit for the green light output. Other six materials are composed of two kinds of lanthanide ions, zeolite, ILs and ligands, which show a variety of different colors. Figure S3(a) and Figure S3 (b) show the selected CIE diagrams for EuW10-IM-[ZA⊃Tb-TAA] (x = 0.5517, y = 0.364) and EuW10-IM-[ZL⊃Tb-TAA] (x = 0.4622, y = 0.4839), respectively, both of which show strong emission of the EuW10. The luminescence color is in the orange region and yellow region, respectively. Figure S1 (c) and (d) show the selected CIE diagrams of TbW10-IM-[ZA⊃Eu-TTA] (x = 0. 41, y = 0.4814) and TbW10-IM-[ZL⊃Eu-TTA] (x = 0.4076, y = 0.5075), as a result of dominant emissive TbW10 and Eu^{3+}, whose luminescence color are green-yellow light. For SmW10-IM-[ZA⊃Tb-TAA] (e) and DyW10-IM-[ZA⊃Tb-TAA] (f), whose CIE coordinates [(x = 0.5962, y = 0.3301) and (x = 0.2869, y = 0.3496)] are in the pale green and orange region, respectively, which is useful for LED. However, by adjusting different components of the materials, we can finally realize the tuning and integration of various luminescence colors.

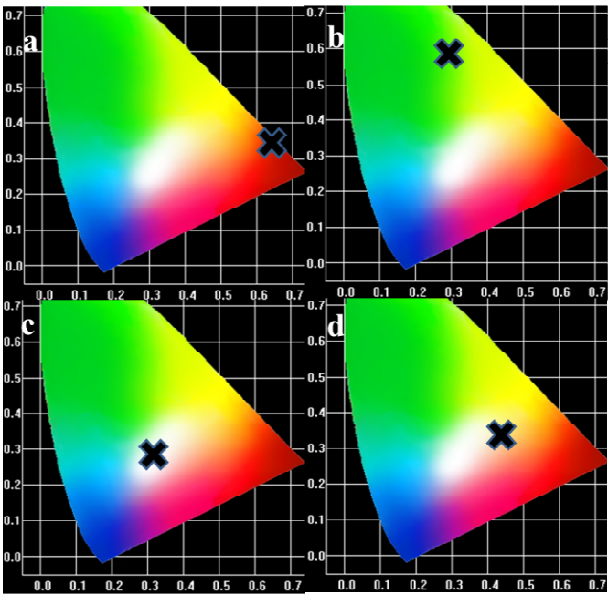

Figure 8 The selected CIE diagrams of hybrid materials: SmW10-IM-[ZA⊃Tb-TAA] (a), TbW10-IM-[ZL⊃Eu-TTA] (b), TbW10-IM-[ZA⊃Eu-TTA] (c) and TbW10-IM-[ZA⊃Tb-TAA] (d)

The outer luminescent quantum efficiency and the luminescent lifetimes of these nine luminescent hybrids are measured, whose data are given in Table 1. It is worthy pointing out that it is hard to show the apparent rule of these multi-component hybrids for they possess complicated composition and different luminescent centers. Here we can only give some comparison from the data. For luminescent lifetimes, EuW10 hybrids present the longer lifetimes than TbW10 hybrids and especially much longer than SmW10 and DyW10 ones. This is in agreement with the luminescent parent LnW10 themselves,

which is due to the existence of internal energy level between the first excited state and ground state of Sm^{3+} and Dy^{3+} to produce the non-radiative energy transfer process. In addition, no apparent distinction can be found for same LnW10 hybrids, whose lanthanide complexes have no big influence on the lifetimes of the whole system. On the other hand, it is even difficult to compare the luminescent quantum efficiencies of these hybrids. Similar to lifetimes of them, EuW10 hybrids possess the highest quantum efficiencies, higher than other hybrid system. In addition, the distinction of hybrids with different zeolite and ligand is not apparent.

Table 1 The luminescence data of the hybrid materials.

Materials	λ_{ex} (λ_{em})	τ (μs)	η (%)
EuW10-IM-[ZA⊃Eu-TTA]	613 (279)	667	43 %
EuW10-IM-[ZA⊃Tb-TAA]	613 (317)	419	31 %
EuW10-IM-[ZL⊃Tb-TAA]	613 (318)	685	49 %
TbW10-IM-[ZA⊃Eu-TTA]	545 (282)	140	8.3 %
TbW10-IM-[ZL⊃Eu-TTA]	545 (276)	159	22 %
TbW10-IM-[ZA⊃Tb-TAA]	545 (285)	154	18 %
SmW10-IM-[ZA⊃Tb-TAA]	600 (292)	57	7.0 %
DyW10-IM-[ZA⊃Eu-TTA]	484 (280)	65	11 %
DyW10-IM-[ZA⊃Tb-TAA]	484 (292)	63	13 %

τ, the luminescent lifetimes ; η, the emission quantum efficiency.

Conclusions

In summary, ionic liquids exchanged lanthanide polyoxometalates and lanthanide beta-dieketonates functionalized zeolite A/L are assembled through the inside-outside double modification paths to nine kinds of multi-component photofunctional hybrid materials. IM^{+} behaves as a bridge to connect the lanthanide polyoxometalates and functionalized zeolite A/L and all these constitutional units are chemically linked in the whole stable hybrid system. These hybrids exhibit strong characteristic luminescence of different lanthanide species, whose various light color and favorable luminescent lifetime or quantum efficiency can be expected to have potential application in practical fields.

Acknowledgements

This work is supported by the National Natural Science Foundation of China (91122003) and the Developing Science Funds of Tongji University.

Notes and references

Department of Chemistry, Tongji University, Shanghai 200092, China. Fax: +86-21-65981097; Tel: +86-21-65984663; E-mail: byan@tongji.edu.cn

Electronic Supplementary Information (ESI) available: The XRD of prepared zeolite A and L, the selected FTIR spectrum and the CIE diagrams of the hybrids. See DOI: 10.1039/b000000x/

1 (*a*) K. Binnemans, *Chem. Rev.*, 2009, **109**, 4283; (*b*) L. D. Carlos, R. A. S. Ferreira, V. D. Bermudez and S. J. L. Ribeiro, *Adv. Mater.*, 2009, **21**, 509; (*c*) B. Yan, *RSC Adv.*, 2012, **2**, 9304; (*d*) J. Feng, H. J. Zhang, *Chem. Soc. Rev.*, 2013, **42**, 387.

2 (*a*) L. D. Carlos, R. A. S. Ferreira, V. D. Bermudez, B. Julian-Lopez and P. Escribano, *Chem. Soc. Rev.*, 2011, **40**, 536; (*b*) R. J. B. Pinto, L. D. Carlos, P. A. A. P. Marques, A. J. D. Silvestre and C. S. R. Freire, *J. Appl. Polym. Sci.*, 2014, 131, 41169; (*c*) P. P. Lima, F. A. A. Paz, C. D. S. Brites, W. G. Quirino, C. Legnani, M. Costa e Silva, R. A. S. Ferreira, S. A. Junior, O. L. Malta, and M. Cremona, *Org. Electr.*, 2014, **15**, 798.

3 (*a*) Z. Li, G. Luppi, A. Geiger, H. P. Josel and L. De Cola, *Small*, 2011, **7**, 3193; (*b*) G. De Cremer, B. F. Sels, J. i. Hotta, M. B. Roeffaers, E. Bartholomeeusen, E. Coutiño - Gonzalez, V. Valtchev, D. E. De Vos, T. Vosch and J. Hofkens, *Adv. Mater.*, 2010, **22**, 957; (*c*) S. V. Eliseeva and J. C. G. Bunzli, *Chem. Soc. Rev.*, 2010, **39**, 189.

4 (*a*) Q. G. Meng, P. Boutinaud, H. J. Zhang and R. Mahiou, *J. Lumin.*, 2007, **124**, 15; (*b*) Y. Li and B. Yan, *Microporous Mesoporous Mater.*, 2010, **128**, 62; (*c*) Duan T. W. and B. Yan, *CrystEngComm*, 2014, **16**, 3395.

5 (*a*) X. M. Guo, H. D. Guo, L. S. Fu, H. J. Zhang, R. P. Deng, L. N. Sun, J. Feng and S. Dang, *Microporous Mesoporous Mater.*, 2009, **119**, 252; (*b*) B. Yan and Y. Li, *Dalton Trans.*, 2010, **39**, 1480; (*c*) Y. J. Li and B. Yan, *Dalton Trans.*, 2010, **39**, 2554; (*d*) M. R. Felicio, T. G. Nunes, P. M. Vaz, A. M. P. Botas, P. Ribeiro-Claro, R. A. S. Ferreira, R. O. Freire, P. D. Vaz, L. D. Carlos and C. D. Nunes, *J. Mater. Chem. C*, 2014, **2**, 9701.

6 (*a*) X. M. Guo, H. D. Guo, L. S. Fu, R. P. Deng, W. Chen, J. Feng, S. Dang and H. J. Zhang, *J. Phys. Chem. C*, 2009, **113**, 2603; (*b*) Y. Li, B. Yan and Y. J. Li, *Microporous Mesoporous Mater.*, 2010, **132**, 87; (*c*) Y. J. Li,L.Wang and B.Yan, *J. Mater. Chem.*, 2011, **21**, 1130.

7 (*a*) X. F. Qiao, H. Y. Zhang and B. Yan, *Dalton Trans.*, 2010, **39**, 8882; (*b*) L. Guo, B. Yan and K. Sheng, *Dalton Trans.*, 2011, 40, 632; (*c*) X. F. Qiao and B. Yan, *J. Phys. Chem. B*, 2009, **113**, 11865; (*d*) B. Yan, L. M. Zhao, X. L. Wang and Y. Zhao, *RSC Adv.*, 2011, **1**, 1064.

8 (*a*) M. Pauchard, S. Huber, R. MeÂallet-Renault, H. Maas, R. Pansu and G. Calzaferri, *Angew. Chem. Int. Ed.*, 2001, 40, 2839; (*b*) N. Gfeller, S. Megelski and G. Calzaferri, *J. Phys. Chem. B* 1999, **103**, 1250; (*c*) G. Calzaferri, H. R. Li and D. Bruhwiler, *Chem. Eur. J.*, 2008, **14**, 7442; (*d*) L. Chen and B. Yan, *Inorg. Chem. Commun.*, 2014, **43**, 75.

9 (*a*) P. P. Cao, Y. G. Wang, H. R. Li and X. Y. Yu, *J. Mater. Chem.*, 2011, **21**, 2709; (*b*) Y. Wang, Y. G. Wang, P. P. Wang, Y. N. Li and H. R. Li, *CrystEngComm*, 2011, **13**, 177.

10 (*a*) J. N. Hao and B. Yan, *Dalton Trans.*, 2014, **43**, 2180; (*b*) J. N. Hao and B. Yan, *New J. Chem.*, 2014, **38**, 3540.

11 (*a*) J. P. Hallett and T. Welton, *Chem. Rev.*, 2011, **111**, 3508; (*b*) N. V. Plechkova and K. R. Seddon, *Chem. Soc. Rev.*, 2008, **37**, 123; (*c*) P. Hapiot and C. Lagrost, *Chem. Rev.*, 2008, **108**, 2238

12 J. S. Wilkes and M. J. Zaworotko, *J. Chem. Soc. Chem. Commun.*, 1992, 965.

13 (*a*) Y. H. Liu, X. Q. Sun, F. Luo and J. Chen, *Anal. Chim. Acta*, 2007, **604**, 107; (b) M. A. Neouze, J. Le Bideau, F. Leroux and A. Vioux, *Chem. Commun.*, 2005, 1082..

14 (*a*) H. R. Li, H. F. Shao, Y. G. Wang, D. S. Qin, B. Y. Liu, W. J. Zhang and W. D. Yan, *Chem. Commun.*, 2008, 5209; (*b*) Z. Y. Yan and B. Yan, *New J. Chem.*, 2014, **38**, 2604.

15 (*a*) Q. P. Li and B. Yan, *Dalton Trans.*, 2012, **41**, 8567; (*b*) Q. P. Li and B. Yan, *RSC Adv.*, 2012, **41**, 10840; (*c*) Y. Mei, Y. Lu and B. Yan, *New J. Chem.*, 2013, **37**, 2619; (*d*) J. Cuan and B. Yan, *Photochem. Photobiol. Sci.*, 2014, **13**, 1469.

16 (*a*) J. Iball, J. N. Low and T. J. R. Weakley, *J. Chem. Soc., Dalton Trans.*, 1974, 2021; (*b*) M. J. Stillman and A. J. Thompson, *J. Chem. Soc., Dalton Trans.*, 1976, 1138; (*c*) H. Li, H. Zhang, L. Wang, D. Mu, S. Qi, X. Hu, L. Zhang and J. Yuan, *J. Mater. Chem.*, 2012, **22**, 9338.

17 (*a*) W. Xu, Q. H. Luo, H. Wang, L. C. Francesconi, R. E. Stark and D. L. Akins, *J. Phys. Chem. B*, 2003, **107**, 497; (b) X. Zhang, C. Zhang, H. Guo, W. Huang, T. Polenova, L. C. Francesconi and D. L. Akins, *J. Phys. Chem. B*, 2005, **109**, 19156; (*c*) H. L. Li, W. Qi, W. Li, H. Sun, W. F. Bu and L. X. Wu, *Adv. Mater.*, 2005, **17**, 2688; (*d*) M. Xu, C. L. Liu, H. L. Li, W. Li and L. X. Wu, *J. Colloid Interface Sci.* 2008, **323**, 176.

18 R. D. Peacock and T. J. R. Weakley, *J. Chem. Soc. (A)*, 1971, 1836.

19 (*a*) J. Cuan and B. Yan, *RSC Adv.*, 2013, **3**, 20077; (*b*) J. Cuan and B. Yan, *Microp. Mesop. Mater.*, 2014, **42**, 14230.

20 (*a*) B. Yan and Y. F. Shao, *RSC Adv.*, 2014, **4**, 3318; (*b*) J. Cuan and B. Yan, *RSC Adv.*, 2014, **4**, 1735; (*c*) J. Cuan and B. Yan, *Microp. Mesop. Mater.*, 2014, **183**, 9.

21 (*a*) P. Laine, R. Seifert, R. Giovanoli and G. Calzaferri, *New. J. Chem.*, 1997, **21**, 453; (*b*) A. Z. Ruiz, D. Bruhwiler, T. Ban and G. Calzaferri, *Monatsh. Chem.*, 2005, **136**, 77.

22. J. F. Dubreuil and J. P. Bazureau, *Tetrahedron Lett.*, 2000, **41**, 7351.

23 (*a*) L. Chen and B. Yan, *Dalton Trans.*, 2014, **43**, 14123; (*b*) L. Chen and B. Yan, *Photochem. Photobiol. Sci.*, 2015, **43**,

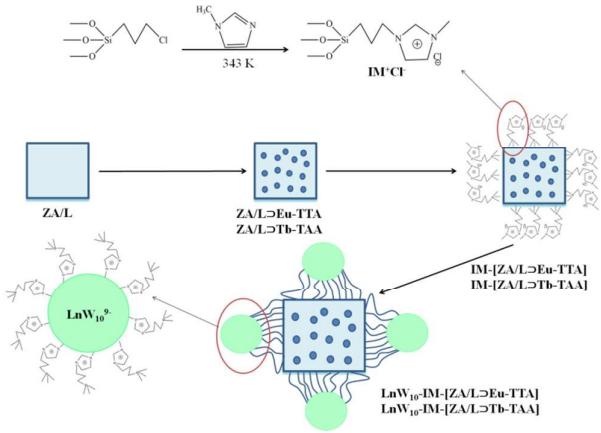

A novel inside-outside double modification path is used to functionalize ZA/L to construct multi-component hybrids presenting multi-color luminescence.

Supporting information

Multi-component assembly and luminescence tuning of lanthanide hybrids through the inside-outside double modification of zeolite A/L

Lei Chen, Bing Yan*

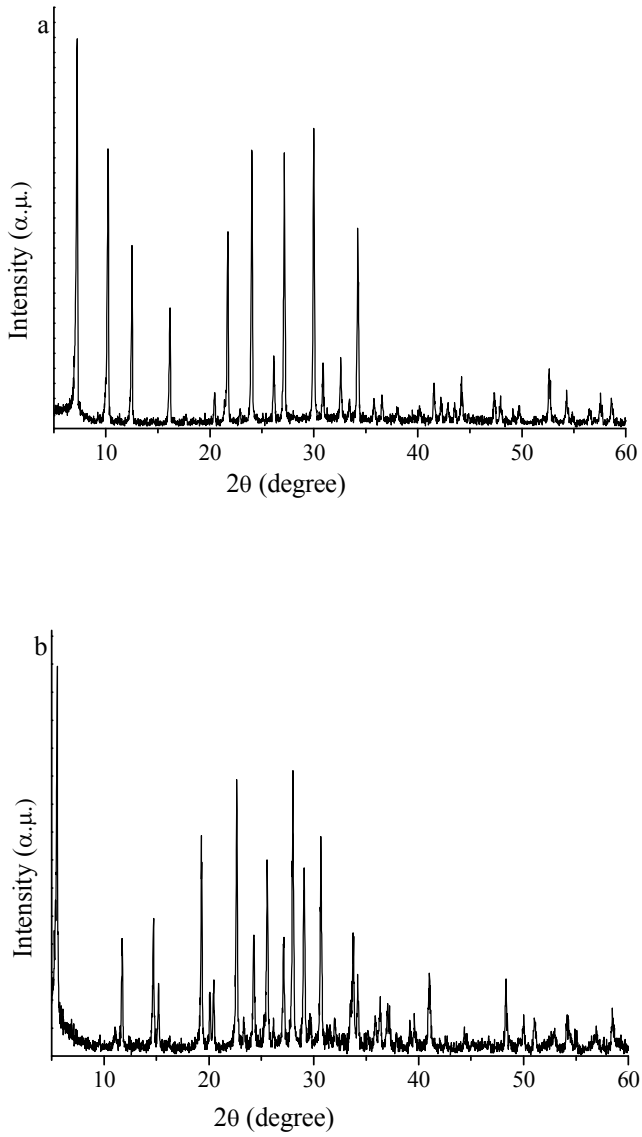

Figure S1 XRD patterns of zeolite A (a) and zeolite L (b) from 5-60 ^{o} in a 2θ range

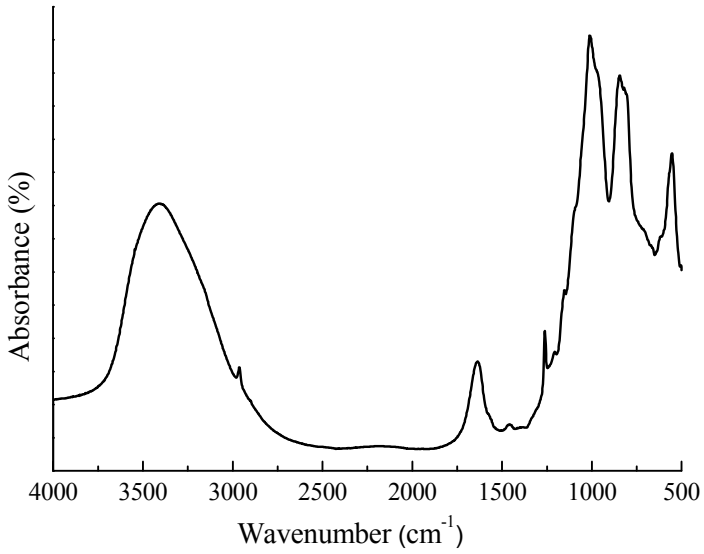

Figure S2 The selected FTIR spectrum of SmW10-IM-[ZA⊃Eu-TTA]

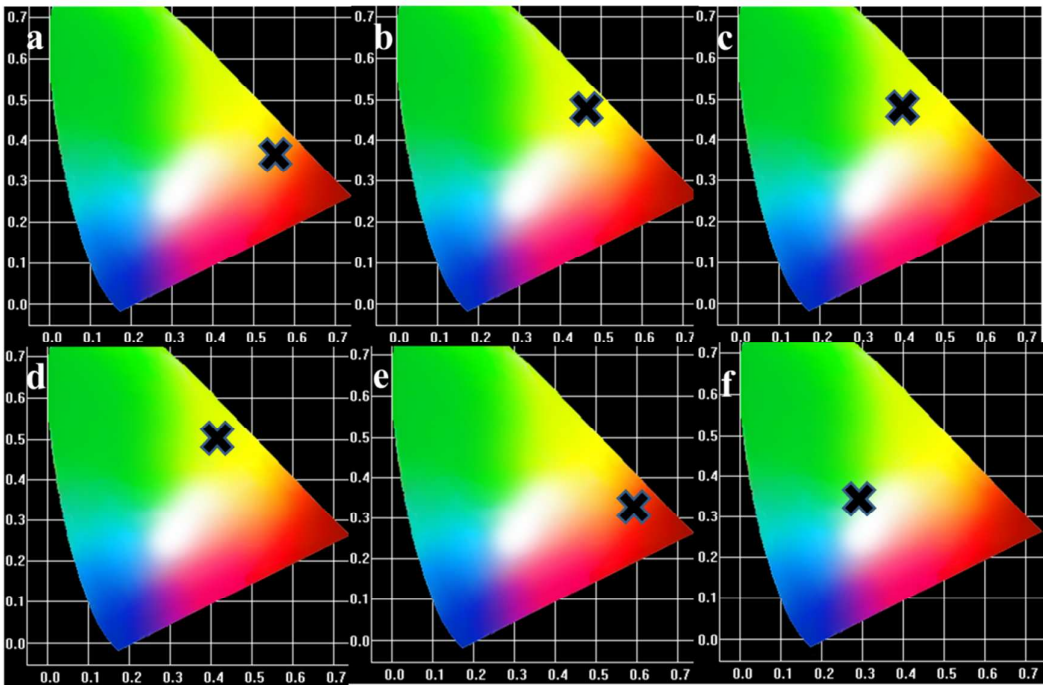

Figure S3 The selected CIE diagrams of EuW10-IM-[ZA⊃Tb-TAA] (a), EuW10-IM-[ZL⊃Tb-TAA] (b), TbW10-IM-[ZA⊃Eu-TTA] (c), TbW10-IM-[ZL⊃Eu-TTA] (d), SmW10-IM-[ZA⊃Eu-TTA] (e) and DyW10-IM-[ZA⊃Tb-TAA] (f)